scientific reports

Check for updates

OPEN

Non-contact lensless holographic reconstruction of diffractive intraocular lenses profiles

Rosa Vila-Andrés[1,2✉], Anabel Martínez-Espert[1,2], Walter D. Furlan[1,2], José J. Esteve-Taboada[1,2] & Vicente Micó[1,2]

A lensless compact arrangement based on digital in-line holography under Gabor's regime is proposed as a novel contactless method to assess the profile of multifocal intraocular lenses (MIOLs) which are conformed by several diffractive rings. Diffractive MIOLs are a widely adopted ophthalmologic option for the correction of presbyopia in patients undergoing cataract surgery. The MIOL optical design might introduce non-negligible optical performance differences between lenses as well as the introduction of undesirable photic phenomena (such as halos and glare) affecting the vision of users. Therefore, the customized topographic control of each manufactured MIOL model, along with the advancement of optical simulation routines, is increasingly necessary to provide users with optimized performance of these implanted optics, as well as predictable and realistic expectations of their future vision with these solutions. In this manuscript, experimental results of the reconstruction of different smooth and highly edged diffractive profiles from a pair of commercially available MIOLs are presented. Besides, a study evaluating the convergence and robustness of the proposed iterative phase-retrieval routine based on a modified classical Gerchberg-Saxton algorithm is performed. These results provide experimental validation of the proposed technique for accurately measuring the optical profiles of MIOLs.

Cataract surgery is one of the most commonly performed surgical procedures worldwide among individuals in middle and later adulthood. Its main purpose is to enhance vision of patients affected by a progressive opacification of the crystalline lens, which ends up with its replacement by a manufactured intraocular lens (IOL). The optical power and characteristics of the lens is usually adapted to patients regarding their ocular parameters and their visual refractive state[1–3]. Hence, there are several IOL designs available on the market that can be classified according to the number of foci they generate, and the optical principle used in their design. For instance, monofocal IOLs had been historically used in cataract surgery for crystalline replacement. However, the increasing visual requirements of patients and the purpose of providing clear vision at several distances without the need of spectacles, contact lenses or other additional optometric compensations, have led clinicians to the implantation of multifocal intraocular lenses (MIOLs). In this way, MIOLs can compensate presbyopia, an age-related accommodation disorder that causes blurred vision at short distances[4], along with distance refractive errors, providing clear vision at various distances.

The multifocality of MIOLs can be achieved through the creation of optical surfaces based on refractive or diffractive profiles which allow to create either a different number of foci at several axial distances or an extended depth-of-focus (EDOF) performance with a clear intermediate range of vision achieved through the newest commercial designs[2,5]. Nevertheless, it is worth noting that choosing the most suitable lens implantation for each patient requires the understanding of the optical performance related to the different available designs. Regarding this aspect, several studies suggest a potential relationship between several types of surface profiles of MIOLs and the presence of quite common but also uncomfortable visual disturbances known as photic phenomena. These visual fluctuations, such as halos and glare, tend to affect users after the surgical MIOL implantation. For instance, higher power additions, as well as highly diffractive surface profiles, have been recently deemed to introduce higher undesirable halos in the visual field of patients[6–9]. As a result, novel technologies based on visual simulators have been recently developed in order to permit patients to experience real-time accurate simulations of their future vision in a previous stage before the MIOLs implantation[10,11]. Consequently, the informed decision of patients can be considered before the beginning of the surgical procedure, thus providing clinical results that match the ones individually expected in a realistic way[12]. Some of the commercially available

[1]Faculty of Physics, Department of Optics and Optometry and Vision Sciences, Universitat de València, Burjassot, Spain. [2] Rosa Vila-Andrés , Anabel Martínez-Espert, Walter D. Furlan, José J. Esteve-Taboada, and Vicente Micó contributed equally to this work. ✉email: rosa.vila@uv.es

current methods include the utilization of systems based on tunable optics, which simultaneously form near and far field images in retina at high temporal frequencies, thus simulating the behavior of MIOLs.

Other similar devices are based on adaptive optics schemes and allow to reproduce phase profiles generated by different lenses designs on a conjugated plane of the pupil of patients[13,14]. These systems work with prior knowledge of the optical surface of each lens design and the related phase distribution induced in retina, which can be determined by publicly available data from manufacturers and from physical measurements[13,15]. This information is crucial for visual simulations of future implanted lenses, offering valuable insights for both patients and clinicians. The reported results appear to accurately reproduce the simulated expectations in most cases[16,17].

Another important application of the physical measurement of the MIOLs optical profile is the quality control during the manufacturing process. This issue constitutes a key aspect since induced variations of the manufactured surfaces differing from theoretical designs can introduce non-negligible and non-expected changes in the implanted lens behavior. In addition, having access to the independent phase profile of each manufactured lens could provide even more reliable information about its individual future visual performance in the eye.

Moreover, several techniques have been described in the literature as successful tools for the inspection and measurement of surface-related characteristics of IOLs. Some of them involve, up to our knowledge, the use of commercially available profilometers and adapted topographers[18–20], atomic force (AFM)[21–23], scanning electron (SEM)[23,24] and confocal[25] microscopy techniques, phase measuring deflectometric methods[26], wavefront reconstruction as Hartmann-Shack[27], laser ray tracing aberrometry[15] and quadriwave lateral shearing interferometry[28], as well as interferometric arrangements based on white-light[29,30], Fizeau[31], and optical coherence tomography (OCT)[32]. However, each of these methods has its own drawbacks. Focusing on microscopic methods and their image recording aspects, the utilization of objective lenses would require, in general, a great number of recordings to inspect the desired field of view (FOV) of the whole IOL. Measurements coming from aberrometers might become restricted to sensing lower frequencies, that is, for smooth wavefronts, yielding in a lower spatial resolution level. Considering interferometry techniques, double-path interferometric arrangements are more sensible to external medium perturbations compared with common-path interferometry. And contact measurement methods (such as AFM and contact profilometers) involve contact procedures that may subject the lens surface and its haptics to physical stress and potential damage. The IOLs composition require their conservation in a liquid medium that ensures the stability of the manufactured structure, so measurements performed in air should be completed in the shortest possible time to preserve the material and morphology of the inspected IOL. Although preliminary holographic approaches have been proposed by other researchers in order to retrieve phase data from IOLs, the proposed configurations require a high amount of recordings in order to perform phase retrieval iterative routines, need a great amount of hardware devices and lack of compactability[33].

In this paper, we address the introduction of digital in-line holography (DIH) under its most classical lensless and one-path configuration as a very compact, single-shot and contactless method to obtain the topographic reconstruction of the diffractive profile of two commercially available MIOLs. This holographic technique, firstly introduced by Dennis Gabor in 1948[34], has been previously validated as a suitable tool in quality control of visual optics materials for the visualization and morphologic characterization of transparent engraving marks performed in peripheral small areas outside the optical zone during the manufacturing of ophthalmic and contact lenses[35–37]. The addressed working principle is based on recording the interference over a photographic plate (substituted by a digital sensor in current configurations[38]) of a non-diffracted reference beam (R), coming from a coherent source of light passing without being disturbed through the sample (in this case, the MIOL) and an object beam (O) caused by diffraction of the illumination when passing through the sample. As a result, this interference creates a hologram (H) whose intensity can be described as $|R+O|^2=|R|^2+|O|^2+ R^*O+RO^*$ (where the asterisk denotes the complex conjugate). Considering phase objects, the object beam must classically introduce a small perturbation of the beam deemed as the reference one and, under these conditions, it is possible to reconstruct accurate phase information.

As a result of the recorded interference, and making use of numerical propagation methods for the diffracted light field traveling through free space, an in-focus image of the sample can be retrieved at a distance z from the sensor, and its related optical phase information ($\Delta\phi$) directly related to the optical path difference (OPD), is introduced as a combination of the geometrical thickness of the inspected sample (ΔL) and the refractive index step between the object and the surrounding medium (Δn) as $\Delta\phi = \frac{2\pi}{\lambda} \cdot \Delta L \cdot \Delta n$[39,40]. Consequently, for a sample with a known refractive index, its related topographic information could be obtained by direct translation of the retrieved optical phase data measured at the sample plane. Nevertheless, because of the one-path in-line arrangement, an identical image of the sample (referred to as "twin image") also appears at the opposite sign distance (-z) from the sensor. Both terms in this configuration will appear overlapped, thus affecting the possible reconstruction of the sample by disturbing the measured phase values and hindering the quality of images[41]. Phase disturbances due to twin image presence (and other coherent artefacts) preventing accurate phase object reconstruction was one of the historically challenging aspects to be addressed in in-line holography. Nevertheless, these limitations consider theoretical phase objects with random phase shifts and their reconstruction through direct propagation to the object plane[42,43]. Nowadays, several and widely described digital methods exist, some of them coming from modified/adapted versions of the classical iterative Gerchberg-Saxton algorithm in order to remove or minimize the twin image contribution and allow a highly reliable phase retrieval in the corresponding sample plane[35,44–53].

In the following sections, the suitability of the proposed DIH approach is explored for the obtention of MIOLs topographies coming from the measured optical phase distribution of a pair of commercially available MIOLs with different diffractive surfaces: Acriva Trinova (VSY Biotecnology, The Netherlands) and FineVision POD F

(PhysIOL, Liege, Belgium). The lens Acriva Trinova is composed of a first smooth sinusoidal surface whereas the FineVision shows a sawtooth profile constituting one of the most diffractive surface distributions currently available in commercial designs of MIOLs. These two cases explore the results and limitations of the application of DIH in this novel and significant field. In addition, an experimental validation regarding the accuracy and convergence of an iterative phase-retrieval routine based on a modified classical Gerchberg-Saxton algorithm is applied to the reconstruction of phase information and twin image removal over the real sample plane to validate the measured results with the publicly available analytical surface information from both analyzed lenses.

Methods

Inspected lenses

Two commercially available MIOLs with two different diffractive patterns have been inspected. The measured lens models, whose main characteristics are described in Table 1, have been the Acriva Trinova (VSY Biotecnology, The Netherlands) and the FineVision POD F (PhysIOL, Liege, Belgium). The former one consists of a trifocal lens provided by a harmonic sinusoidal diffractive pattern with 12 concentric rings distributed alongside an optical size of 6 mm. This pattern is disposed on the anterior surface of the lens with a mean nominal height of 0.84 µm, thus adding intermediate and near distance additions of + 1.50 D and + 3.00 D, respectively, to its base power[25,54]. The latter one offers addition values of + 1.75 D and + 3.50 D through a diffractive anterior surface design composed of 26 concentric rings on an equal optical size. This specific design is based on two apodized and well differentiated sawtooth diffractive patterns whose related rings are disposed in interleaved order along the anterior surface[29,30,55,56]. The apodization of the FineVision lens is radially symmetric, and it is defined by the progressive reduction in diffractive step heights from the center to the periphery. This height variation is usual in MIOLs design so as to modify the energy used at each focus, resulting in a lens whose energy efficiency at each focus depends on the pupil size of the patient. If no apodization is used and the diffractive step heights are one wavelength high, the lens would behave in monofocal fashion and all the light would be concentrated in a single focus at the first diffraction order. Similarly, when the steps are a half wavelength high, light is approximately distributed into the first and zero diffraction orders. For other step-height values, the energy is divided in accordance with the 2 diffraction orders.

Experimental assembly

Figure 1 shows the experimental optical setup used in this experiment. It consists of a coherent source of light provided by a divergent pigtailed diode laser coupled to a single mode fibre (Blue Sky Research, SpectraTec STEC4-405/450/532/635nm) from which the 532 nm wavelength is selected. This value is in the center of the visible range spectrum and is the one nearest to the manufacturing design values, thus providing the best optical performance in visual optics systems.

The illumination beam reaches the MIOLs that, regarding their porous structure, have been placed inside a horizontally disposed quartz cuvette filled with saline solution (n_s=1.34 for the used wavelength) to preserve their morphologic properties. The cuvette counts with a lens holder that has a circular diaphragm of 6.0 mm of diameter. This element ensures a static position of the lenses preventing them from decentrations and tilts while providing an equally illuminated optical area for the lenses.

Next to the cuvette, a digital CMOS sensor (Basler daA2448-70 µm, 2448 × 2048 pixels, 2.74 μm pixel width) is used to record the hologram. Finally, recorded images are numerically processed by a commercial laptop (HP Pavilion x360 14-ek2001ns, 16 GB RAM, 512 GB SSD, 12th Gen Intel® Core i7, Intel iRISxe graphics).

Measuring conditions were previously defined in Zemax Optic Studio (v.18.7, LLC, Kirkland WA, USA). In the proposed arrangement, the light source is conveniently located at the far object focus plane of the multifocal system formed by the lens and the saline-filled cuvette. The assembly distance from the source to the first wall of the cuvette depends on the base optical power of the MIOL, being 53.5 mm for the Acriva Trinova lens and 71.5 mm for the FineVision lens. This configuration ensures, firstly, a beam parallel to the optical axis of the system associated with the far-distance highest optical power plane (thereby providing a lateral magnification of $M = 1$ over the recording sensor). And secondly, both diffraction beams corresponding to the intermediate and short-distance power additions of the lenses become two additional convergent beams illuminating the CMOS digital sensor. This sensor is placed at 5 mm distance from the cuvette to optimize resolution limit and avoid energy

	FineVision POD F	Acriva Trinova
Optical design	Trifocal diffractive, aspheric	Trifocal sinusoidal, aspheric
Optical base power (D)	+ 13.00	+ 17.00
Material	Hydrophilic (26%) acrylic. UV and blue-light blocker	Hydrophilic and hydrophobic acrylic copolymer
Optical diameter (mm)	6.00	6.00
Spherical aberration (µm)	0.11	-
Refractive Index (n_s) (Design wavelenght)	1.46 (550 nm)	1.46 (546 nm)
Abbe Number	58.00	58.00
Difractive rings	26	12

Table 1. Optical characteristics of the measured MIOLs[25,30,54–56].
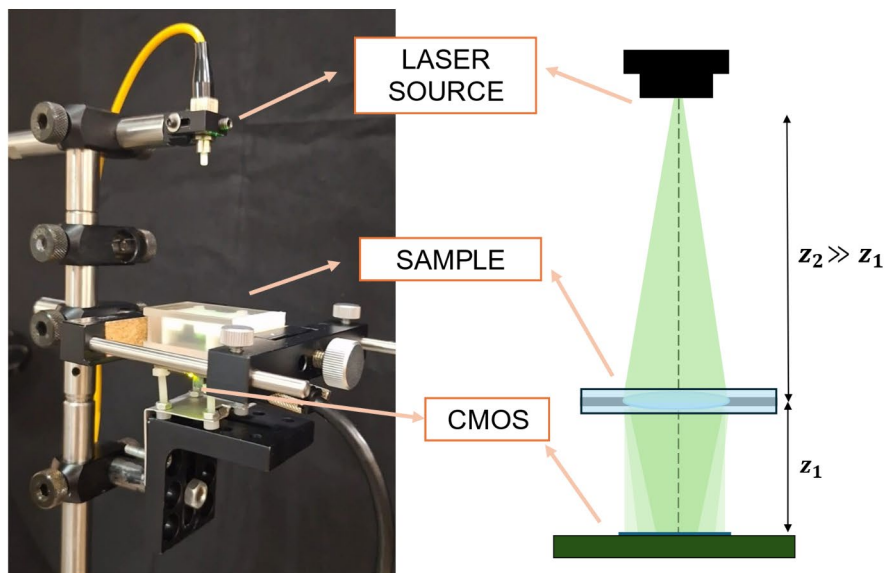
Fig. 1. Experimentally assembled DIH optical setup for MIOLs measurement: picture at the lab (left) and basic scheme of the layout (right).

focalization coming from the two additional foci of the lenses. A simulated example of this optical configuration for the Acriva Trinova lens is depicted in Fig. 2, where the sequential mode in Zemax OpticStudio was employed.

Regarding the resolution limits of the proposed experimental configuration, on the one hand, the Nyquist's theorem establishes a sampling resolution limit (ρ_s) of twice the size of the pixel pitch of the CMOS, that is, $\rho_s = 5.5$ μm. This is consequence of the magnification factor M = 1 of the optical configuration (otherwise, the magnification factor would affect proportionally the resolution limit). And on the other hand, the diffraction-limited resolution value ($\rho_d = \lambda / NA$) being NA the numerical aperture) become $\rho_{d1} = 2.37$ μm when considering a NA related with a full diameter of 6.0 mm[40]. That way, the achieved resolution limits comprise the one required for the spatial resolution of the target rings, including the most peripheral ones for the Acriva Trinova (~100 μm) and FineVision POD F (~50 μm) lenses.

Hologram recording, digital image processing and height computation

Considering the robustness to external perturbations provided by the one-path configuration and given that the lateral magnification and FOV over the sensing area covered all the diffraction area coming from the region of interest, a single hologram has been recorded for each one of the lenses. The acquired interference data has been processed in MATLAB 2023a (The MathWorks, Inc., Natick, MA, USA). An initial digital back propagation from the recorded hologram to the real object plane provides an in-focus image of the target sample. Hence, to numerically assess digital propagation of light, the chosen kernel has been the angular spectrum (AS) based propagator[40]. AS relies on the approximation of the propagated wavefront onto flat waves due to the light source location ensuring the compensation of the main optical power of samples and considering a collimated outgoing beam. This stage helps to avoid the introduction of undesirable defocus effects in the reconstruction process. However, the reduced optical size of both lenses permits to assume quasi-flat sagittal values for the inspected surfaces. In addition, optical phase data can be retrieved from the real object plane of the recorded holograms after numerical back propagation from the hologram plane. This information can be directly translated into OPD and subsequently to geometrical height steps (that are found on the measured surface). For this conversion, the corresponding refractive index steps between the sample and the surrounding medium need to be known.

Moreover, an iterative phase-retrieval routine, a modified Gerchberg-Saxton algorithm (a widely described method in literature[35,40]), has been conducted in order to assess an efficient optical phase recovery on the object plane and a proper cancellation of disturbing twin image contributions. This iterative routine allows to accurately estimate the optical phase values on the object plane starting from known intensity (I_0) available in the recorded hologram. The performance of this algorithm, which is represented in Fig. 3, consists of several back-and-forth numerical propagations between the hologram and the real object planes. For the first cycle, the routine starts assuming, on the hologram plane, only the initial amplitude of the recorded signal and a null phase value $U_0 = A_0 = (I_0)^{1/2}$.
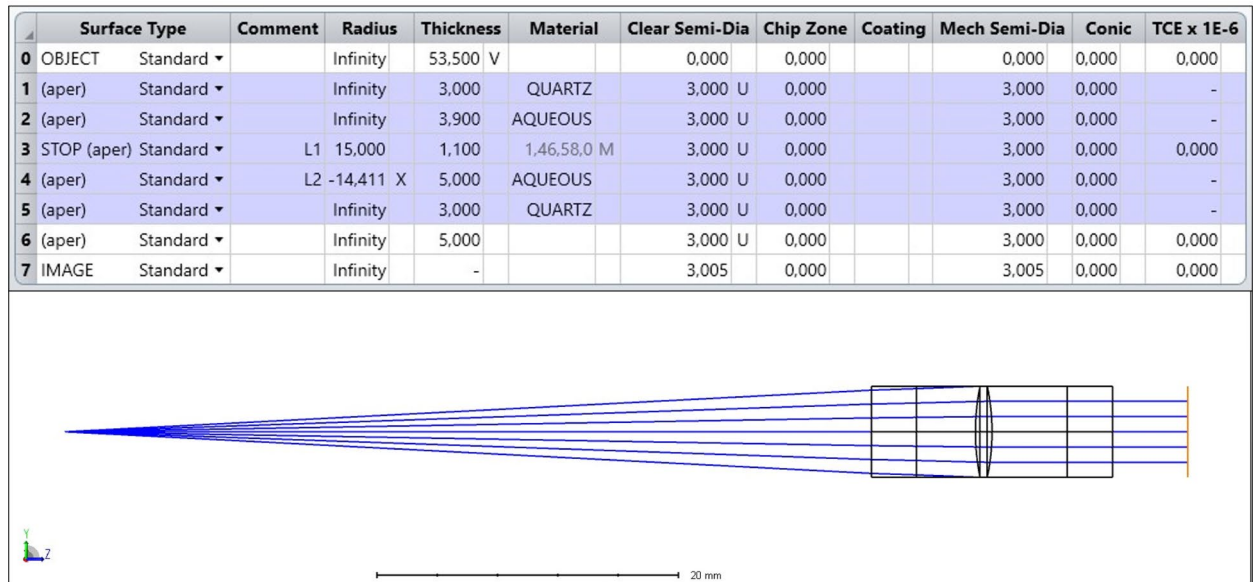
	Surface Type		Comment	Radius	Thickness	Material	Clear Semi-Dia	Chip Zone	Coating	Mech Semi-Dia	Conic	TCE x 1E-6
0	OBJECT	Standard ▾		Infinity	53,500 V		0,000	0,000		0,000	0,000	0,000
1	(aper)	Standard ▾		Infinity	3,000	QUARTZ	3,000 U	0,000		3,000	0,000	-
2	(aper)	Standard ▾		Infinity	3,900	AQUEOUS	3,000 U	0,000		3,000	0,000	-
3	STOP (aper)	Standard ▾	L1	15,000	1,100	1,46,58,0 M	3,000 U	0,000		3,000	0,000	0,000
4	(aper)	Standard ▾	L2	-14,411 X	5,000	AQUEOUS	3,000 U	0,000		3,000	0,000	-
5	(aper)	Standard ▾		Infinity	3,000	QUARTZ	3,000 U	0,000		3,000	0,000	-
6	(aper)	Standard ▾		Infinity	5,000		3,000 U	0,000		3,000	0,000	0,000
7	IMAGE	Standard ▾		Infinity	-		3,005	0,000		3,005	0,000	0,000

Fig. 2. Zemax OpticStudio simulation of the experimental configuration distances and the resulting performance for the far-distance optical base power of the Acriva Trinova lens.
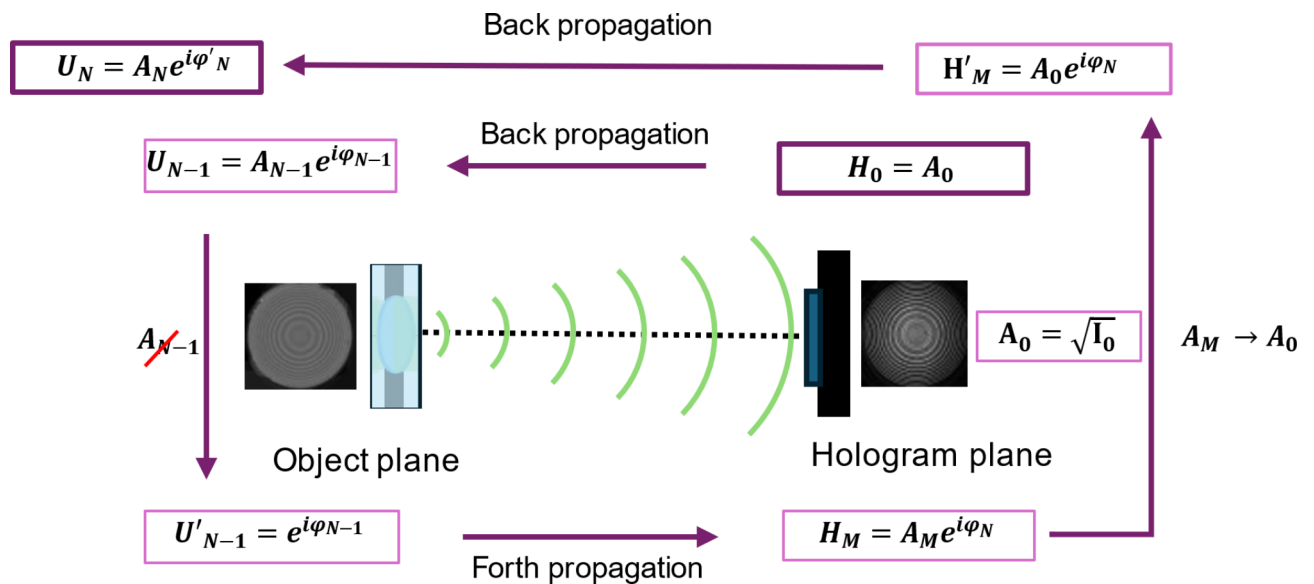
Fig. 3. Diagram of the modified Gerchberg-Saxton algorithm procedure (see the main text for details).

Once this initial field is backpropagated to the object plane using the AS propagation kernel, the resulting complex distribution $U_N = A_N \cdot e^{i\phi}$ is constricted to assume in this plane the presence of a pure phase object. As a result, the related amplitude term is cancelled, and the signal becomes simplified to only the exponential complex term ($U_N{'} = e^{i\phi}$). This new $U_N{'}$ distribution is forth propagated to the hologram plane yielding a complex amplitude distribution $H_M = A_M \cdot e^{i\phi'}$ containing a first iteration of a tentative phase term (φ') as a result of the numerical propagation of $U_N{'}$ to the hologram plane. Finally, the amplitude of this newly obtained hologram is substituted by the initial recorded one ($H_M{'} = A_0 \cdot e^{i\phi'}$) and $H_M{'}$ becomes the input for a new set of iterations repeating the same described steps until the loop is stopped at a specific number of iterations.

The number of cycles may vary depending on the desired accuracy of the final optical phase estimation and other aspects such as the diffractive nature of the sample. Consequently, a study of the height-estimated values convergence obtained with different number of iterations of the modified Gerchberg-Saxton has been conducted comparing the number of iterations in a range from 100 to 10,000 cycles and the related mean height of the diffractive rings obtained for both lenses. After ending the phase retrieval routine, optical phase (φ) was translated to height (L) as $\Delta L = \frac{\lambda}{2\pi \cdot \Delta n} \cdot \Delta\phi$, and for enhancing the results, the background of the obtained height maps has been subtracted from the reconstructions in the Fourier domain, and the averaged profile obtained from radial cuts covering the 360º range of both lenses has been computed. Finally, a curve (using the "envelope" function in Matlab) comprising the averaged values of the upper and lower envelopes that are tangent to those profiles has been subtracted from the reconstructed signals. This step ensures the background of the retrieved profiles to remain centered at zero and prevents them to be affected by residual wavefront distortions.

Once the final profile has been obtained, the height steps are calculated as the retrieved values from the phase steps considering the difference between peaks and valleys of the rings. This difference was then divided by two for comparison purposes with previous literature[25]. The aim of this procedure is to look for the most suitable number of iterations ensuring that the mean and standard deviation computed values for height comprise the theoretical values without experimenting significant variations. This would confirm that the algorithm outputs do converge through several iterations and would consequently prove the robustness of the phase retrieval technique.

Results
Topographic measurements
Figures 4 and 5 show the obtained topographies and surface profiles expressed in microns for the two inspected MIOLs, Acriva Trinova and FineVision lenses, respectively. The number of iterations of the modified Gerchberg-Saxton algorithm used to depict the reconstructions is 600, since it has been deemed the minimum number of iterations needed to obtain a robust and time-balanced reconstruction of the proposed topographies.

More specifically, Fig. 4 (A) and 5 (A) show the recorded holograms, while Fig. 4 (B)−5 (B) and 4 (C)−5 (C) represent, respectively, the initial bidimensional (2D) height maps and the finally computed tridimensional (3D) topographies obtained after the subtraction of their corresponding backgrounds and the compensation of remaining residual wavefront distortions. In addition, the final 360º averaged radial profile of each lens is shown in Fig. 4 (D)−5 (D). The peaks and valleys of the measured optical profile (blue and green plots) are contrasted with the theoretical profiles (purple plots) for easier comparison. As it can be seen, the retrieved data closely aligns with the theoretical curves for both lenses. Specifically, our approach successfully reconstructs around 10 diffractive rings for the Acriva Trinova lens, and around 13 diffractive rings for the FineVision lens.
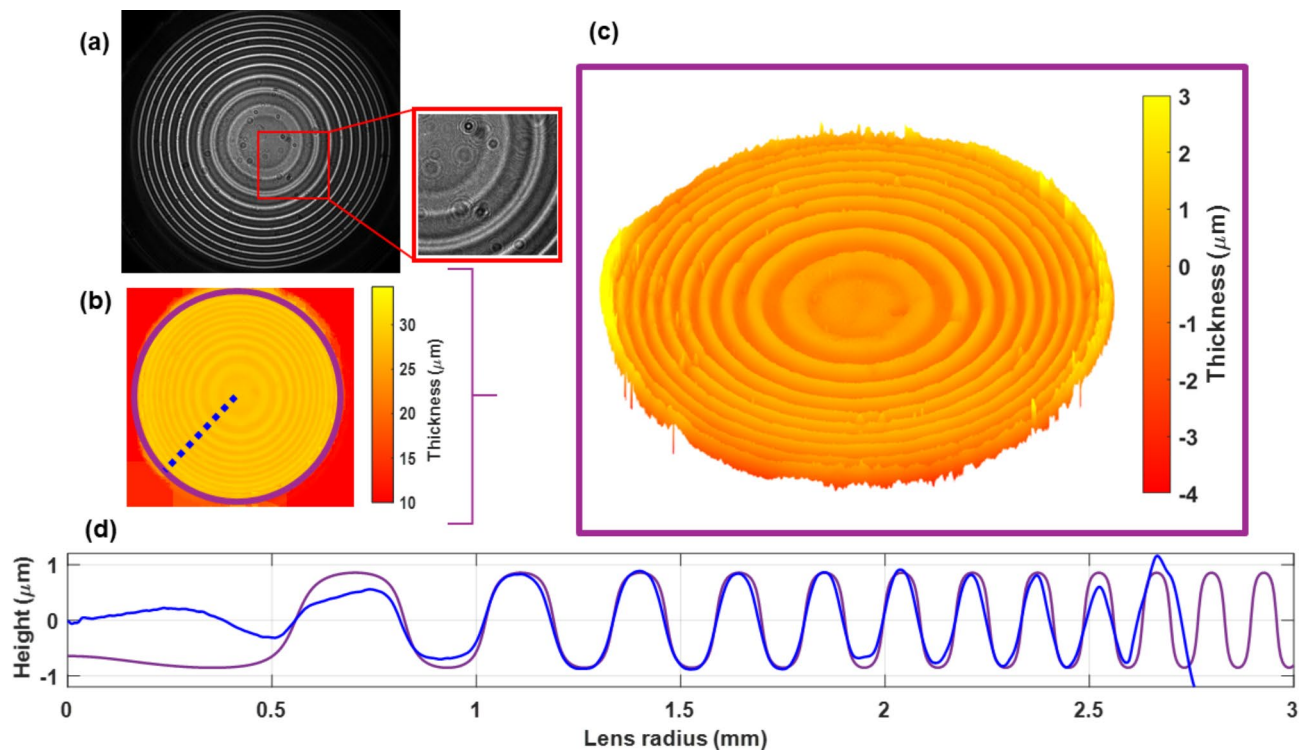

Fig. 4. Acriva Trinova lens results: (**A**) Recorded hologram and a magnified section. (**B**) Initial 2D thickness map. (**C**) 3D view of the obtained topography. (**D**) Comparison of the experimentally measured profile (blue line) with the theoretical one[25] (purple line).
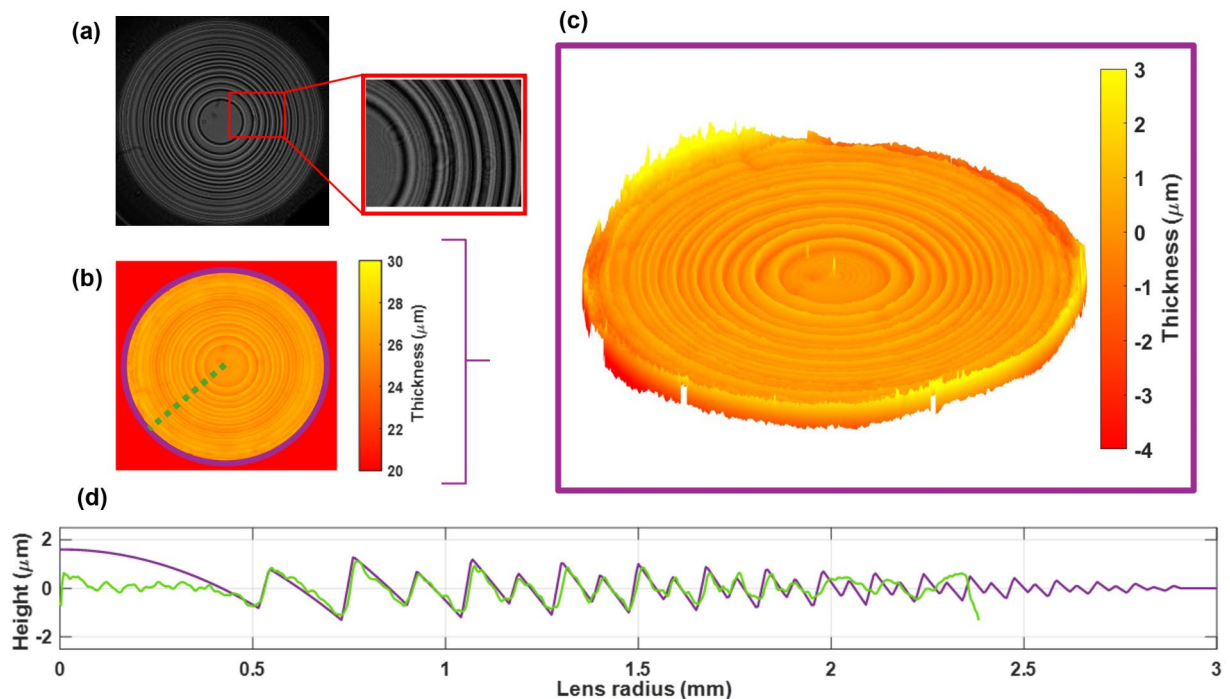
Fig. 5. FineVision POD F lens results: (**A**) Recorded hologram and a magnified section. (**B**) Initial 2D thickness map. (**C**) 3D view of the obtained topography. (**D**) Comparison of the experimentally measured profile (green line) with the theoretical one[29] (purple line).

Going a bit deeper, the Acriva Trinova lens shows a smoother sinusoidal surface profile than the FineVision one, and it is almost approaching the border of the lens in the reconstruction where only the two outer rings are not properly resolved (probably because of diffraction effects in the circular lens frame that impairs the measurement). However, the FineVision lens is quite different than the Acriva Trinova one, because this lens constitutes a highly diffractive surface with a periodic structure composed by two substructures having different sawtooth profiles with attenuated height towards lens periphery. For this case, the proposed approach is capable of properly reconstructing 13 of these ring structures arriving almost to recover a radius of 2 mm. This value is a bit lower than the Acriva Trinova lens, since the phase steps introduced by the elements at such radius are on the same level as the coherent noise of the reconstructions which hinders the characterization of those structures.

Algorithm convergence

Figure 5 shows the experimentally validated performance of the modified Gerchberg-Saxton algorithm applied to the obtention of the height values of both examined lenses. Figure 5 (A) shows the computation time as a function of the number of iterations, while the results depicted at Fig. 5 (B) and 6 (C) show the lens profiles obtained by averaging the retrieved height data considering radial profiles from the center to the periphery along 360º for the Acriva Trinova and FineVision MIOLs, respectively. These results consider 10 reconstructed peaks of the Acriva Trinova lens and the first 12 reconstructed rings of the FineVision one. As a result, it can be noticed a strong convergence obtained in a range starting at a minimum number of 600 algorithm cycles to 10000 iterations. Estimated heights values for 600 iterations are 0.79 ± 0.14 µm for Acriva Trinova lens, and 0.68 ± 0.23 µm for FineVision POD F lens, and 0.77 ± 0.15 µm, and 0.67 ± 0.25 µm for 10000 iterations, respectively. While almost all the values are quite similar for 600 and 10000 iterations in both averaged profiles, the standard deviations for the FineVision lens show higher values fairly introduced by the two well differentiated diffracting apodized patterns included in the lens profile (as depicted in Fig. 5). Consequently, we can conclude that 600 iterations are the proper number of iterations needed to obtain a robust and time-balanced reconstruction of the proposed topographies.

Discussion

The aim of this study was to demonstrate, for the first time, that DIH can successfully be employed to obtain topographic data from diffractive profiles in MIOLs. In our preliminary results, height maps and averaged radial cuts have been successfully recovered for two MIOLs with very different diffractive profiles: the Acriva Trinova lens (with a sinusoidal profile), and the FineVision POD F lens (a lens that combines two bifocal diffractive profiles). Our results align closely with the theoretical diffractive profiles provided by the manufacturers. The comparison has been validated in terms of global shape and averaged height for the inspected diameter (close to 6 mm for the Acriva Trinova lens and close to 4 mm for the FineVision lens). The morphologic profile of
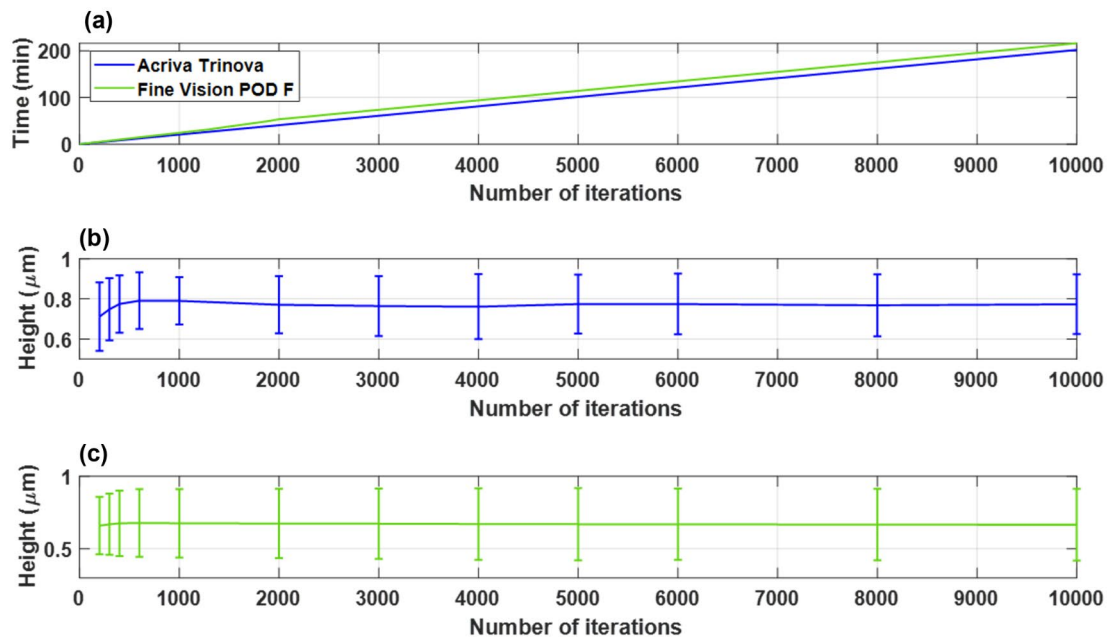
Fig. 6. Convergence results for the modified Gerchberg-Saxton phase-retrieval algorithm used in the study. (**A**) Computation time corresponding to a different number of iterations of the algorithm. (**B**) Mean height values for the Acriva Trinova lens measured rings. (**C**) Mean height values for the FineVision POD F lens measured rings.

the diffractive rings constitutes the main target in our application, since those structures are added to the base curvature of the lens which may vary depending on the optical power required for the far vision correction of each user. Thus, the diffractive profile remains invariant between lenses and defines two power additions for the assessment of intermediate and near distance vision, independent of far vision correction. Therefore, characterizing the diffractive profile is highly significant in the modern manufacturing of MIOLs.

The introduction of this methodology offers a novel tool for the obtention of the 3D profiles in a completely contactless testing environment that permits to achieve an individual characterization of lenses while ensuring the preservation of their surface and materials. The retrieved data could help clinicians predict the optical performance of each manufactured lens by considering specific differences introduced by manufacturing processes from the theoretical profiles. Moreover, the utilization of a lensless and one-path holographic configuration provides a very compact and cost-effective technique with great robustness to medium-related disturbances in comparison with other interferometric techniques. Furthermore, it is also suitable for the reconstruction of non-smooth edged surface profiles that can suppose a challenging target for wavefront-sensing based instruments. As a result, the proposed technique could be practically adapted and implemented both separately or in combination with other quality control arrangements as optical benches used to study the optical performance of lenses[57,58]. In addition, the obtained height values can be exported to computer simulation programs and visual simulators to perform digital calculations of the potential performance of each lens under different controlled conditions (aberrated corneas, tilts, decentrations, etc.).

A common drawback present in lensless arrangements working in a non-telecentric scheme would be the introduction of residual wavefront distortions, especially when the assumption of local flatness of the reconstructed wavefronts is applied to the inspected samples[59]. Hence, related issues were reported in previous studies where lensless DIH technology was implemented for the characterization of engravings located in strongly curved contact lenses and where defocus and distortion effects restricted the inspection to local areas[37]. Nevertheless, this issue has been successfully overcome by the introduction of numerical processing techniques involving background subtraction from the reconstructed phase maps and compensation of residual distortions associated with each individually retrieved profile. Moreover, the initial collimation of the far-distance power ensures an outgoing flat wavefront propagating from the sample to the sensor regardless the general high base power of MIOLs, whose surface sagittas are also assumed as quasi-flat in accordance with the power of lenses and their reduced diameter. These reconstructions are provided with a convenient FOV with a lateral magnification close to one, also involving a single shot measuring process that would allow to record the region of interest through only one snapshot (unlike other approaches that work with higher lateral magnification values requiring several images to cover the same lens area). Nonetheless, different magnification values could also be used to perform similar results. For instance, the characterization of specific surface defects found in the

surface of MIOLs would require higher magnification so as to enhance lateral resolution, whereas larger samples with a wider FOV would need smaller values[60–62].

Regarding resolution constraints for the characterization of MIOLs' rings, the resolution limit of the optical system perfectly fulfils the spatial requirements of the proposed samples. The major limitation comes from the geometry of the digital sensor (sampling constraint) since the diffraction-limited resolution of the system becomes significantly lower. Details about those limits are provided in the experimental assembly description along the Methods section.

Probably, the most notably affected region of the inspected MIOLs is the peripheral area falling close to the edge of the sensing digital area. Those rings might have been affected by the introduction of noise, probably related to stray light and undesirable diffraction coming from the diaphragm edge. This aspect affects specifically the reconstruction of the profile of the Acriva Trinova lens depicted in Fig. 4, being one of the reasons for not resolving the outer rings. In addition, the retrieved profile of the FineVision lens shows a decrease in the peripheral area when compared to the theoretical profile from a radius up to 2 mm (as shown in Fig. 5). In this case, this effect is probably due to the apodized surface profile in the lens design, making lower the height of the rings in this lens from the center to its periphery. The reconstruction of such tiny peripheral rings could be affected by phase noise coming from the inherent coherent nature of the proposed layout. This issue is a commonly reported aspect in coherent imaging techniques employing laser sources such as DIH, and could be enhanced through the introduction of partially coherent sources in future arrangements[35,63,64].

In addition, some inaccuracies are noticeable in the central recovery area of lenses, thus coinciding with the center of both lenses and the first ring for the Acriva Trinova. It is worth noting that the center of lenses was outside our reconstruction target since it varies depending on the optical base power of the inspected lens. Nevertheless, the retrieval of the lowest spatial frequencies is a current challenging aspect in DIH. Previous researches in DIH using algorithms based on the Gerchberg-Saxton, have reported some issues in the recovery of low spatial frequencies in the inspected samples[65], thus coinciding with the center of both lenses as well as for the first ring for the Acriva Trinova. Moreover, inaccuracies in the retrieval of the central area of IOLs have previously been reported in optical power reconstruction maps using commercially available deflectometric devices[66].

Another aspect that should be taken into further consideration would be the computing time associated with a different number of iterations in the phase-retrieval routine. This challenging aspect should be optimized in future research to provide an optimal performance of the algorithm, and it could be addressed by the study of different results provided by other phase-retrieval approaches. Nevertheless, the proposed modified Gerchberg-Saxton algorithm has shown high robustness along a wide range of iterations (from 600 up to 10000). The retrieved height values obtained become comparable with other experimental approaches that had previously reported similar mean height measurements using confocal microscopy $(0.78 \pm 0.10$ μm$)$[25] for the Acriva Trinova lens. Moreover, the standard deviation related to the FineVision mean height measurements is slightly increased. This can be explained by the presence of two different surface patterns in the second lens and a decreasing height alongside the lens radius whereas the computed mean is performed for all the rings. These calculations aim to introduce a convergence metric of the algorithm reassuring that equal heights for equal areas are obtained through a different number of iterations. The accuracy of the retrieval is examined by comparing individually the retrieved lens profile with the theoretical one in both lenses. Thus, it is worth noting that for the calculations performed on the Acriva Trinova lens, the first retrieved ring is also considered. This ring shows the least accuracy in the measurements. Additionally, if an equal calculation procedure is followed without considering the central ring, that is, from the second to the tenth ring, a lower standard deviation is obtained with a mean height closer to the theoretical one, thus becoming 0.83 ± 0.07 μm the computed height for 600 cycles and 0.81 ± 0.10 μm for 10000.

In conclusion, the proposed DIH scheme working under Gabor's regime and a lensless and contactless environment has demonstrated a robust performance to the reconstruction of smooth as well as abrupt diffractive optical profiles of MIOLs. Nevertheless, some practical aspects can be further considered in order to decrease the coherent source of noise affecting the lowest height steps close to the phase sensitivity accuracy, especially for apodized lenses (such as the FineVision one). Additionally, different digital phase-retrieval approaches could be explored to even further optimize computation time requirements of the reported technique.

Data availability

All data required to reproduce the results can be obtained from the corresponding author upon a reasonable-request.

References

1. Rampat, R. & Gatinel, D. Multifocal and extended depth-of-focus intraocular lenses in 2020. *Ophthalmology* **128**, e164–e185. https://doi.org/10.1016/j.ophtha.2020.09.026 (2021).
2. Salerno, L., Tiveron, M. & Alió, J. Multifocal intraocular lenses: types, outcomes, complications and how to solve them. *Taiwan. J. Ophthalmol.* **7**, 179–184. https://doi.org/10.4103/tjo.tjo_19_17 (2017).
3. Zvornicˇanin, J. & Zvornicˇanin, E. Premium intraocular lenses: the past, present and future. *J. Curr. Ophthalmol.* **30**, 287–296. https://doi.org/10.1016/j.joco.2018.04.003 (2018).
4. Wolffsohn, J. S., Davies, L. N. & Sheppard, A. L. New insights in presbyopia: impact of correction strategies. *BMJ Open. Ophthalmol.* **8**, e001122. https://doi.org/10.1136/bmjophth-2022-001122 (2023).
5. MacRae, S. et al. Special report: American academy of ophthalmology task force consensus statement for extended depth of focus intraocular lenses. *Ophthalmology* **124**, 139–141. https://doi.org/10.1016/j.ophtha.2016.09.039 (2017).

6. Alba-Bueno, F., Vega, F. & Millán, M. S. Halos Y lentes intraoculares multifocales: Origen E interpretación. *Arch. de la. Sociedad Esp. De Oftalmol.* **89**, 397–404. https://doi.org/10.1016/j.oftal.2014.01.002 (2014).

7. Serdiuk, V., Ustymenko, S., Fokina, S. & Ivantsov, I. Comparison of three different presbyopia-correcting intraocular lenses. *Romanian J. Ophthalmol.* **64** https://doi.org/10.22336/rjo.2020.58 (2020).

8. Adre, E. & Tonk, R. Positive and negative dysphotopsias: causes, prevention, and best strategies for treatment. *Curr. Ophthalmol. Rep.* **9**, 1–10. https://doi.org/10.1007/s40135-021-00278-w (2021).

9. Pusnik, A., Petrovski, G. & Lumi, X. Dysphotopsias or unwanted visual phenomena after cataract surgery. *Life* **13** https://doi.org/10.3390/life13010053 (2023).

10. Furlan, W. D. et al. Optical performance of a new design of a trifocal intraocular lens based on the devil's diffractive lens. *Biomed. Opt. Express.* **14**, 2365–2374. https://doi.org/10.1364/boe.487812 (2023).

11. Gargallo, D. et al. Multi-toric optical element to compensate ocular astigmatism with increased tolerance under rotation. *Opt. Lett.* **49**, 2289–2292. https://doi.org/10.1364/OL.518973 (2024).

12. Marcos, S. et al. Simulating outcomes of cataract surgery: important advances in ophthalmology. *Annu. Rev. Biomed. Eng.* **23**, 277–306. https://doi.org/10.1146/annurev-bioeng-082420-035827 (2021).

13. Vinas, M. et al. Visual simulators replicate vision with multifocal lenses. *Sci. Rep.* **9,** 1539. https://doi.org/10.1038/s41598-019-38673-w (2019).

14. Marcos, S. et al. Adaptive optics visual simulators: a review of recent optical designs and applications [invited]. *Biomed. Opt. Express.* **13**, 6508–6532. https://doi.org/10.1364/boe.473458 (2022).

15. Akondi, V. et al. Evaluation of the true wavefront aberrations in eyes implanted with a rotationally asymmetric multifocal intraocular lens. *J. Refract. Surg.* **33**, 257–265. https://doi.org/10.3928/1081597X-20161206-03 (2017).

16. Barcala, X. et al. Comparison of vision with multifocal contact lenses and simvis gekko simulations in a clinical site. *Investig Ophthalmol. Vis. Sci.* **61**, 579–579 (2020).

17. Vinas, M. et al. Optical and visual quality with physical and visually simulated presbyopic multifocal contact lenses. *Transl Vis. Sci. Technol.* **9**, 20–20. https://doi.org/10.1167/tvst.9.10.20 (2020).

18. Kannengießer, M., Zhu, Z., Langenbucher, A. & Janunts, E. Evaluation of free-form iol topographies by clinically available topographers. *Z. Med. Phys.* **22**, 215–223. https://doi.org/10.1016/j.zemedi.2012.04.002 (2012).

19. Moschitta, D. & Schwiegerling, J. Single-shot intraocular lens surface measurement with the gelsight topography system. 268–285, (2022). https://doi.org/10.1117/12.2632400

20. Miret, J. J., Camps, V. J., García, C., Caballero, M. T. & Gonzalez-Leal, J. M. Analysis and comparison of monofocal, extended depth of focus and trifocal intraocular lens profiles. *Sci. Rep.* **12**, 8654. https://doi.org/10.1038/s41598-022-12694-4 (2022).

21. Lombardo, M., Talu, S., Talu, M., Serrao, S. & Ducoli, P. Surface roughness of intraocular lenses with different dioptric powers assessed by atomic force microscopy. *J. Cataract Refract. Surg.* **36**, 1573–1578. https://doi.org/10.1016/j.jcrs.2010.06.031 (2010).

22. Giacinto, C. D. et al. Surface properties of commercially available hydrophobic acrylic intraocular lenses: comparative study. *J. Cataract Refract. Surg.* **45**, 1330–1334. https://doi.org/10.1016/j.jcrs.2019.04.011 (2019).

23. Son, H., Lee, J., Khoramnia, R. & Choi, C. Comparative surface imaging study of multifocal diffractive intraocular lenses. *Klin. Monatsbl. Augenheilkd.* **239**, 982–990. https://doi.org/10.1055/a-1328-2550 (2022).

24. Brockmann, T. et al. Scanning electron microscopic characteristics of commercially available 1- and 3-piece intraocular lenses. *J. Cataract Refract. Surg.* **39**, 1893–1899. https://doi.org/10.1016/j.jcrs.2013.04.046 (2013).

25. Vega, F., Valentino, M., Rigato, F. & Millán, M. S. Optical design and performance of a trifocal sinusoidal diffractive intraocular lens. *Biomed. Opt. Express.* **12**, 3338–3351. https://doi.org/10.1364/boe.421942 (2021).

26. Speck, A., Zelzer, B., Kannengießer, M., Langenbucher, A. & Eppig, T. Inspection of freeform intraocular lens topography by phase measuring deflectometric methods. *Appl. Opt.* **52**, 4279–4286. https://doi.org/10.1364/AO.52.004279 (2013).

27. Kannengießer, M., Langenbucher, A. & Janunts, E. Individual iol surface topography analysis by the wavemaster reflex uv.*BioMed Res. Int.* 363742, (2013). https://doi.org/10.1155/2013/363742 (2013).

28. Baffou, G. Wavefront microscopy using quadriwave lateral shearing interferometry: from bioimaging to nanophotonics. *ACS Photonics.* **10**, 322–339. https://doi.org/10.1021/acsphotonics.2c01238 (2023).

29. Gatinel, D., Pagnoulle, C., Houbrechts, Y. & Gobin, L. Design and qualification of a diffractive trifocal optical profile for intraocular lenses. *J. Cataract Refract. Surg.* **37**, 2060–2067. https://doi.org/10.1016/j.jcrs.2011.05.047 (2011).

30. Loicq, J., Willet, N. & Gatinel, D. Topography and longitudinal chromatic aberration characterizations of refrac- tive–diffractive multifocal intraocular lenses. *J. Cataract Refract. Surg.* **45**, 1650–1659. https://doi.org/10.1016/j.jcrs.2019.06.002 (2019).

31. Mencucci, R., Menchini, U., Volpe, R., Vannoni, M. & Molesini, G. Intraocular lenses with surface aspherization: interferometric study. *J. Cataract Refract. Surg.* **33**, 1624–1630. https://doi.org/10.1016/j.jcrs.2007.05.028 (2007).

32. Wu, Q., Wang, X., Liu, L. & Mo, J. Inspection of intraocular lens with dual-side view optical coherence tomography. *IEEE Photonics J.* **13**, 1–10. https://doi.org/10.1109/JPHOT.2021.3080498 (2021).

33. Ryu, J. Estimation of Diffractive Surface Profile using Phase Retrieval TechniquesDoctoral dissertation, University of Arizona,. (2023).

34. Gabor, D. A new microscopic principle, DOI: 10.1038/161777a0 (1948).

35. Perucho, B. & Micó, V. Wavefront Holoscopy: application of digital in-line holography for the inspection of engraved marks in progressive addition lenses. *J. Biomed. Opt.* **19**, 016017–016017. https://doi.org/10.1117/1.jbo.19.1.016017 (2014).

36. Perucho, B., Picazo-Bueno, J. A. & Micó, V. A novel marking reader for progressive addition lenses based on gabor holography. *Optom. Vis. Sci.* **93**, 534–542. https://doi.org/10.1097/OPX.0000000000000818 (2016).

37. Vila-Andrés, R., Esteve-Taboada, J. J. & Micó, V. Soft contact lens engraving characterization by wavefront holoscopy. *Sensors* **24**, 3492. https://doi.org/10.3390/s24113492 (2024).

38. Xu, W., Jericho, M. H., Meinertzhagen, I. A. & Kreuzer, H. J. Digital in-line holography for biological applications. *Proc. Natl. Acad. Sci. United States Am.* 98, 11301–11305, (2001). https://doi.org/10.1073/pnas.191361398

39. Kreis, T. *Handbook of Holographic Interferometry: Optical and Digital Methods* (Wiley-VCH Verlag GmbH Co. KGaA, 2005).

40. Schnars, U., Falldorf, C., Watson, J. & Jüptner, W. *Digital holography and wavefront sensing: Principles, techniques and applications* (2015).

41. Zhang, W. et al. Twin-image-free holography: a compressive sensing approach. *Phys. Rev. Lett.* **121** https://doi.org/10.1103/PhysRevLett.121.093902 (2018).

42. Gabor, D. Microscopy by reconstructed wave-fronts. *Proc R Soc. Lond. Ser. Math. Phys. Sci.* **197**, 454–487 (1949).

43. Gabor, D. Microscopy by reconstructed wave fronts: II. *Proc. Phys. Soc. Sect. B.* **64**, 449 (1951).

44. Latychevskaia, T. Criteria for objects suitable for reconstruction from holograms and diffraction patterns. *J. Opt. Soc. Am. A.* **41**, 2219–2230. https://doi.org/10.1364/JOSAA.534332 (2024).

45. Gerchberg, R. W. & Saxton, W. O. Practical algorithm for the determination of phase from image and diffraction plane pictures. *Optik (Stuttgart).* **35**, 237–246 (1972).

46. Liu, G. & Scott, P. D. Phase retrieval and twin-image elimination for in-line fresnel holograms. *J. Opt. Soc. Am. A.* **4**, 159–165. https://doi.org/10.1364/josaa.4.000159 (1987).

47. Latychevskaia, T. & Fink, H. W. Solution to the twin image problem in holography. *Phys. Rev. Lett.* **98** https://doi.org/10.1103/PhysRevLett.98.233901 (2007).

48. Sanz, M., Picazo-Bueno, J. A., García, J. & Micó, V. Improved quantitative phase imaging in lensless microscopy by single-shot multi-wavelength illumination using a fast convergence algorithm. *Opt. Express.* **23**, 21352–21365. https://doi.org/10.1364/oe.23.021352 (2015).

49. Sanz, M., Ángel Picazo-Bueno, J., Granero, L., García, J. & Micó, V. Four channels multi-illumination single-holographic-exposure lensless fresnel (mishelf) microscopy. *Opt. Lasers Eng.* **110**, 341–347. https://doi.org/10.1016/j.optlaseng.2018.06.020 (2018).

50. Latychevskaia, T. Iterative phase retrieval for digital holography: tutorial. *J. Opt. Soc. Am. A.* **36**, D31–D40. https://doi.org/10.1364/JOSAA.36.000D31 (2019).

51. Chen, L., Singh, R. K., Vinu, R. V., Chen, Z. & Pu, J. A wavefront division multiplexing holographic scheme and its application in looking through diffuser. *New. J. Phys.* **23** https://doi.org/10.1088/1367-2630/ac35a7 (2021).

52. Jin, X. et al. Iterative denoising phase retrieval method for twin-image elimination in continuous-wave terahertz in-line digital holography. *Opt. Lasers Eng.* **152** https://doi.org/10.1016/j.optlaseng.2022.106986 (2022).

53. Micó, V., Rogalski, M., Ángel Picazo-Bueno, J. & Trusiak, M. Single-shot wavelength-multiplexed phase microscopy under Gabor regime in a regular microscope embodiment. *Sci. Rep.* **13**, 4257. https://doi.org/10.1038/s41598-023-31300-9 (2023).

54. Biotechnologie, V. & Product downloads, U. R. L. https://www.vsybiotechnology.com/detail/ophthalmology/healtcare-professionals/our-products/our-inspiring-portfolio/trifocal-iol-s/acriva-trinova

55. Ferreira, T. B. & Ribeiro, F. J. Prospective comparison of clinical performance and subjective outcomes between two diffractive trifocal intraocular lenses in bilateral cataract surgery. *J. Refract. Surg.* **35**, 418–425. 10.3928/ 1081597X-20190528-02 (2019).

56. BVI, M. & Productos URL: https://medicalmix.com/productos/lentes-intraoculares/lente-trifocal/lente-trifocal-pod-finevision/?p=5889

57. Azor, J. A., Vega, F., Armengol, J. & Millan, M. S. Optical assessment and expected visual quality of four extended range of vision intraocular lenses. *J. Refract. Surg.* **38**, 688–697. https://doi.org/10.3928/1081597X-20220926-01 (2022).

58. Montagud-Martínez, D. et al. In vitro chromatic performance of three presbyopia-correcting intraocular lenses with different optical designs. *J. Clin. Med.* **11**, 1212. https://doi.org/10.3390/jcm11051212 (2022).

59. Bogue-Jimenez, B., Trujillo, C. & Doblas, A. Comprehensive tool for a phase compensation reconstruction method in digital holographic microscopy operating in non-telecentric regime. *PLoS ONE.* **18**, e0291103. https://doi.org/10.1371/journal.pone.0291103 (2023).

60. Meier, R. W. Magnification and third-order aberrations in holography. *J. Opt. Soc. Am.* **55**, 987–992. https://doi.org/10.1364/josa.55.000987 (1965).

61. Perraut, F., Doménès, M., Grateau, H. & Josso, Q. Achieving magnification smaller than 1 in lensless microscopy by illumination with a convergent wavefront. *Opt. Lett.* **41**, 5326–5328. https://doi.org/10.1364/ol.41.005326 (2016).

62. Sanz, M., Trusiak, M., García, J. & Micó, V. Variable zoom digital in-line holographic microscopy. *Opt. Lasers Eng.* **127** https://doi.org/10.1016/j.optlaseng.2019.105939 (2020).

63. Dohet-Eraly, J., Yourassowsky, C., Mallahi, A. E. & Dubois, F. Quantitative assessment of noise reduction with partial spatial coherence illumination in digital holographic microscopy. *Opt. Lett.* **41**, 111–114. https://doi.org/10.1364/ol.41.000111 (2016).

64. Remmersmann, C., Stürwald, S., Kemper, B., Langehanenberg, P. & Bally, G. V. Phase noise optimization in temporal phase-shifting digital holography with partial coherence light sources and its application in quantitative cell imaging. *Appl. Opt.* **48**, 1463–1472. https://doi.org/10.1364/AO.48.001463 (2009).

65. Winnik, J., Suski, D., Arcab, P., Rogalski, M. & Trusiak, M. Phase retrieval via conjugate gradient minimization in double-plane lensless holographic microscopy. *Opt. Express.* **32**, 28666. https://doi.org/10.1364/oe.525986 (2024).

66. Gómez-Pedrero, J. A., Albarrán-Diego, C., García-Montero, M., Garzón, N. & Gonzalez-Fernandez, V. Influence of instrumental factors in the Measurement of Power Profiles of Intraocular Lenses with a commercial deflectometer. *Appl. Sci.* **13**, 9882. https://doi.org/10.3390/app13179882 (2023).

Acknowledgements

Author contributions

R.V.-A.: conceptualization, methodology, data curation, formal analysis, software, validation, and writing—original draft.A. M-E.: conceptualization, methodology, data curation, formal analysis, validation, visualization, and writing—reviewdraft. J.E.-T.: conceptualization, data curation, formal analysis, supervision, and writing—review and editing. V.M.: conceptualization, methodology, data curation, formal analysis, software, validation, supervision, writing—original draft.W.D.F.: conceptualization, data curation, formal analysis, supervision, and writing—review and editing.All authors have read and agreed to the published version of the manuscript.

Declarations

Competing interests

The authors declare no competing interests.

Accession codes

All data required to reproduce the results can be obtained from the corresponding author upon a reasonable request.

Additional information

Supplementary Information The online version contains supplementary material available at https://doi.org/10.1038/s41598-024-84363-7.

Correspondence and requests for materials should be addressed to R.V.-A.

Reprints and permissions information is available at www.nature.com/reprints.

Publisher's note Springer Nature remains neutral with regard to jurisdictional claims in published maps and institutional affiliations.